

Research Paper

Cite this article: Du H, Wan F, Lalléchére S, Rahajandraibe W, Ravelo B (2022). Robustness study of bandpass NGD behavior of ring-stub microstrip circuit under temperature variation. *International Journal of Microwave and Wireless Technologies* **14**, 1045–1053. <https://doi.org/10.1017/S1759078721001562>

Received: 11 August 2021
Revised: 24 October 2021
Accepted: 26 October 2021
First published online: 23 November 2021



Key words:

Bandpass NGD; electrothermal analysis; experimentation; microstrip circuit; robustness study; S-parameters analysis; temperature effect characterization

Author for correspondence:

Fayu Wan,
E-mail: fayu.wan@nuist.edu.cn

Robustness study of bandpass NGD behavior of ring-stub microstrip circuit under temperature variation

Hongyu Du¹ , Fayu Wan¹ , Sébastien Lalléchére², Wenceslas Rahajandraibe³ and Blaise Ravelo¹

¹Nanjing University of Information Science & Technology (NUIST), Nanjing 210044, Jiangsu, China; ²Université Clermont Auvergne, Institut Pascal, SIGMA Clermont, Clermont-Ferrand, France and ³Aix-Marseille University, CNRS, University of Toulon, IM2NP UMR7334, Marseille, France

Abstract

This paper explores an original study of bandpass (BP) negative group delay (NGD) robustness applied to the ring-stub passive circuit. The proof of concept (PoC) circuit is constituted by a ring associated with the open-end stub implemented in microstrip technology. An innovative experimental setup of a temperature room containing the NGD PoC connected to a vector network analyzer is described. Then, the electrothermal data of S-parameters are measured by varying the ambient or room temperature range from 20 to 60°C, i.e. 40°C maximal variation. The empirical results of the group delay (GD), transmission and reflection coefficient mappings versus the couple (temperature, frequency) highlight how the temperature affects the BP NGD responses. An innovative electrothermal calibration technique by taking into account the interconnection cable influence is developed. The electrothermal robustness analysis is carried out by variations of the NGD center frequency, cut-off frequencies and value in function of the temperature.

Introduction

The practical existence of the intriguing negative group delay (NGD) effect was initially experimented with by physicists with an optical system [1–4]. In the beginning, the observation of the NGD effect was made by using negative group velocity (NGV) dispersive media [1, 2]. The analytical study of the NGD effect is necessary for the basic physical interpretation. Then, the NGD function existence at the microwave wavelength becomes an attractive topic for electronic design and research engineers [5–12].

The remarkable period of the NGD function development in the microwave area has been found during the design of metamaterial artificial transmission line (TL) exhibiting a negative refractive index effect [5–8]. The metamaterial-based NGD circuits were designed with periodical structures [6, 8]. Diverse microwave NGD devices operating as quad-band circuits [7], reconfigurable circuits with tunable metamaterial resonators [11], and resistive lossy left-handed TLs [12] were proposed. It was emphasized that some NGD circuits are susceptible to propagate pulse signals with superluminal effect [13–16]. Moreover, the superluminal effect was experimented with different systems with optimal behavior [14], two interference pulses [15], and an active circuit approach [16]. Nevertheless, the existence of the NGD function and superluminal effect is not in contradiction with the causality [17, 18]. Such counterintuitive and extraordinary effect observation raises curious questions on the meaning and interpretation of the NGD function in electronic and microwave engineering. Therefore, a simple theorization of the NGD function based on the analogy with the filter function was initiated [19].

Innovative NGD circuits operating with low-pass and bandpass (BP) behaviors were designed. Thanks to the ambitious research work made by some research groups around the world, various topologies of typical BP NGD circuits were investigated [20–29]. The main challenges on the NGD microwave circuit of the last two decades were on the loss compensation [20, 21], circuit operation understanding [22, 23], the size reduction [24–27], and the implementation of low-attenuation passive circuits [28, 29] susceptible to operate in the gigahertz frequency range. An active NGD circuit designed with a microwave transversal filter approach was proposed [20]. To highlight the NGD design feasibility of some microstrip topologies, an absorptive bandstop filter based [21] and signal interference [22] based NGD circuit were introduced. Furthermore, different NGD compact circuits based on microstrip TLs were investigated [24–27]. Then, innovative geometrical shape topologies of low loss NGD passive microstrip circuits were proposed [28, 29]. Some tentative applications of the NGD function targeted for the GD equalization were initiated [30, 31].

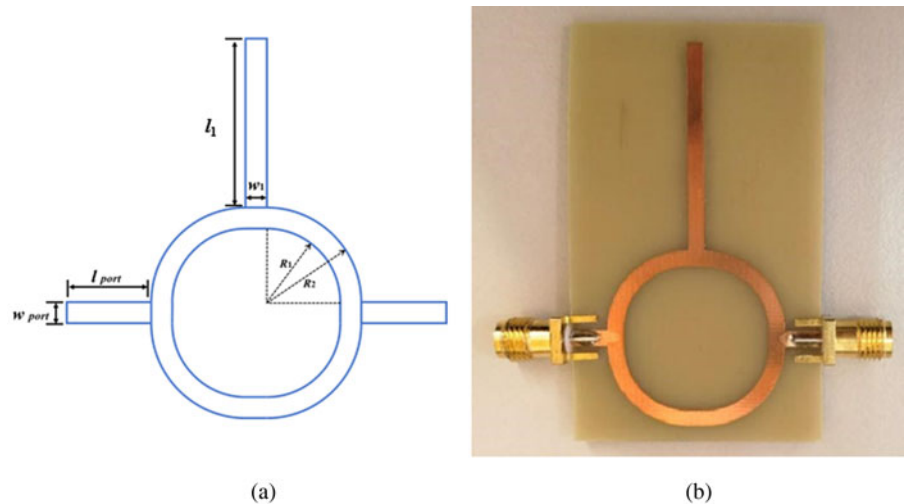


Fig. 1. (a) 2-D design and (b) photo of the ring-stub circuit under study.

Behind the progress of the microwave circuit design, further curious questions remain to be answered. For example, we would like to study the temperature effect on the NGD microstrip circuit as investigated in [32–34]. The paper is organized into four main sections as follows:

- Section II introduces the design of the proof of concept (PoC) of the BP NGD circuit constituted by the combined ring and stub microstrip structure.
- Section III investigates the experimental setup on the BP NGD circuit under test (CUT) of the empirical robustness study. The guideline of the innovative electrothermal test operation process with the calibration technique of the temperature room will be explained.
- Section IV discusses the observable results of the robustness study. The electrothermal empirical results illustrating the NGD performances versus the ambient temperature will be examined which show the variation of the BP NGD responses.
- Then, Section V is the conclusion.

Design description of the ring-stub BP NGD circuit

This section describes the design and implementation of the PoC prototype. The BP NGD circuit is designed by modification of parallel line topology [28]. Then, the performance was optimized by adjusting the location and physical length of the open stub.

Poc of microstrip circuit design

The considered PoC is a two-port distributed passive circuit. As illustrated by the 2-D design shown by Fig. 1(a), the circuit is constituted by two microstrip circular lines presenting physical inner radius, R_1 , outer radius, R_2 and width, w . The two circular lines are connected in parallel. The access lines have physical length, l_{port} and width, w_{port} .

The top circular line is connected to an open-ended straight stub having physical length, l_1 , and width, w_1 , at its mid-point. The physical parameters of this PoC prototype are indicated in Table 1. The fabricated circuit prototype photographed in Fig. 1(b) is implemented on Cu-metalized FR4 dielectric substrate in microstrip technology. The substrate physical characteristics are addressed by Table 2.

Table 1. Geometrical parameters of the circuit PoC

Circuit	Description	Parameters	Values, mm
Whole circuit	Total length	L	58.2
	Total width	w	35
Access line	Length	l_{port}	5
	Width	w_{port}	2.8
Stub	Length	w_1	2.2
	Width	l_1	28
Ring	Inner radius	R_1	9.5
	Outer radius	R_2	11.5

Table 2. Physical parameters of the PoC circuit substrate

Structure	Description	Parameters	Values
Substrate	Relative permittivity	ϵ_r	4.5
	Loss tangent	$\tan(\delta)$	0.02
	Thickness	h	1.6 mm
Metallization conductor	Copper conductivity	σ	58 MS/m
	Thickness	t	35 μm

BP NGD function specification

The analysis of the ring-stub passive symmetric circuit is based on the 2-D frequency-dependent S-matrix:

$$[S(j\omega)] = \begin{bmatrix} S_{11}(j\omega) & S_{21}(j\omega) \\ S_{21}(j\omega) & S_{11}(j\omega) \end{bmatrix} \quad (1)$$

with the angular frequency, ω . The main parameters are basically the transmission coefficient magnitude, and the reflection coefficient, respectively:

$$S_{21}(\omega) = |S_{21}(j\omega)| \quad (2)$$

$$S_{11}(\omega) = |S_{11}(j\omega)| \quad (3)$$

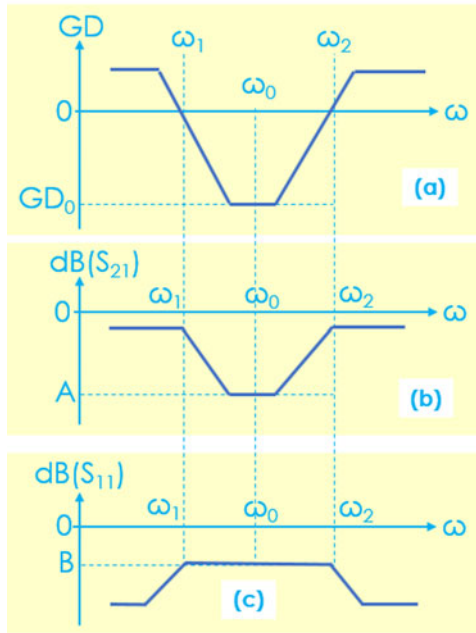


Fig. 2. BP NGD circuit ideal responses: (a) GD , (b) S_{21} and (c) S_{11} .

Then, the essential parameter is the GD defined by:

$$GD(\omega) = -\partial \arg [S_{21}(j\omega)] / \partial \omega \tag{4}$$

Figure 2(a) represents the GD response of BP NGD ideal circuit. This BP NGD function is characterized by the cut-off angular frequencies, $\omega_1 < \omega_2$, with:

$$GD(\omega_1 < \omega < \omega_2) < 0 \tag{5}$$

The associated NGD bandwidth (BW) is given by:

$$\Delta\omega = \omega_2 - \omega_1 \tag{6}$$

The response is also characterized by a center angular frequency $\omega_1 < \omega_0 < \omega_2$ which can be defined by:

$$GD(\omega_0) = GD_0 < 0 \tag{7}$$

The behavior of the transmission coefficient characterized by attenuation limit:

$$S_{21}(\omega_0) = A \tag{8}$$

is presented by Fig. 2(b). Then, the access matching can be limited with respect to the diagram of Fig. 2(c) by:

$$S_{11}(\omega_0) = B \tag{9}$$

These specifications will serve the BP NGD electrothermal characterization in the rest of the paper.

To investigate the electrothermal NGD behavior of the circuit, an innovative experimental setup described in the following section was considered.

Experimental setup of the robustness study applied to the ring-stub circuit

The present section describes the robustness study empirical principle. The PoC of the robustness is based on the electrothermal analysis of the ring-stub NGD circuit. The experimental setup will be introduced in the following subsection.

Principle of the experimental setup for the NGD electrothermal analysis

The electrothermal empirical study principle of microwave circuit is fundamentally aimed to determine the transmission and reflection coefficients of S-matrix proposed in equation (1) with the evolution of ambient temperature, T :

$$[S(jf, T)] = \begin{bmatrix} S_{11}(jf, T) & S_{21}(jf, T) \\ S_{21}(jf, T) & S_{11}(jf, T) \end{bmatrix} \tag{10}$$

It means that the empirical S-parameter data should be expressed in the function of a couple $(j\omega = j2\pi f, T)$. To measure the S-parameters, we proposed the innovative experimental setup highlighted by an illustrative diagram in Fig. 3. The vector network analyzer (VNA) is facing the side of the test box. After calibration, two ports are respectively connected with a 1 m-long cable. The cable enters the test box through the hole on the side of the test box. At the same time, the two cables are relatively parallel and do not cross for a certain distance to avoid mutual interference. After putting it into the test chamber, fix both ends of the cable on the iron frame inside the test chamber with adhesive tape, and fix the thermometer. After placing, close the door of the test chamber to start the test. Of course, the VNA apparatus is needed to record the S-parameters. The thermal room specifications will be described in the following subsection.

Electrothermal test and the thermal room specification

Figure 4 shows the photograph of the electrothermal test setup. The employed VNA is referenced Agilent® AV3672B-S, which operates from 10 to 26.5 GHz. We use two identical SMA cables 1meter-length. Then, the main innovative part of this research work is the consideration of the thermal room with volume $1\text{ m} \times 1\text{ m} \times 1\text{ m}$. This later one is referenced ESPEC® [35]. During the experimentation, the circuit under test (CUT) is placed in the room as indicated in Fig. 4. Then, it is connected to the VNA as previously depicted in Fig. 3. Prior to running the test, the VNA was calibrated in SOLT configuration at the ambient temperature, $T_a = 20^\circ\text{C}$. We underline that the present study is limited to the case of temperature, T , higher than T_a .

Then, we realize that such calibration remains valid to measure the circuit with the variation of the room temperature, $\Delta T = T - T_a < 100^\circ\text{C}$. Moreover, the influence of the room temperature on the interconnection cables and CUT connectors is negligible.

Guideline of the thermal room test operation

The thermal room test operation can be summarized by the following steps:

- Step A: Installation with respect to the diagram shown by Fig. 3. This step requires the familiarization to the use of VNA and the

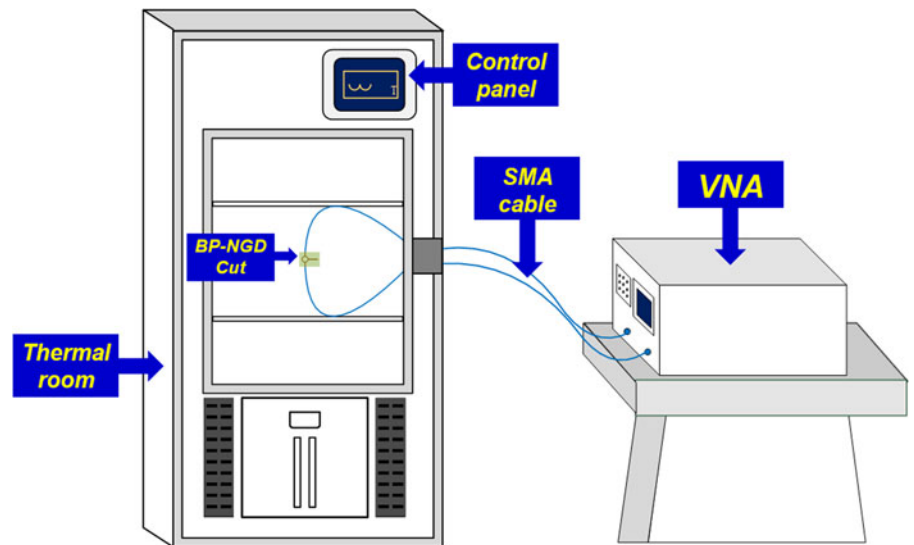


Fig. 3. Schematic diagram of NGD electrothermal test device.

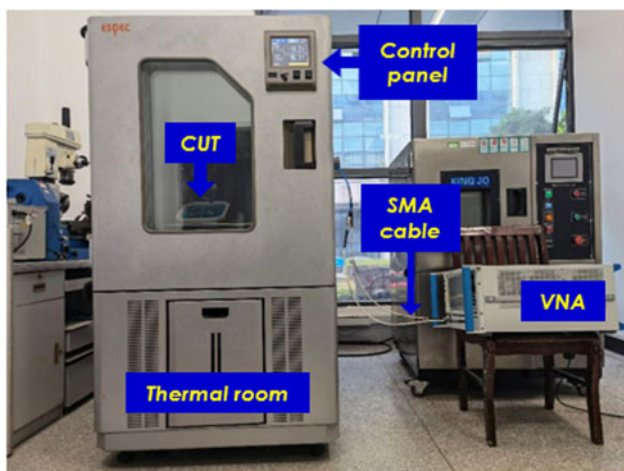


Fig. 4. Photo of the considered electrothermal experimental setup.

control of the temperature (alternating humidity and heat) with the thermal test chamber.

- *Step B:* Connect the extension cable and put it into the high and low temperature (alternating humidity and heat) test chamber without a test circuit to ensure that the two cables entering the temperature chamber are equal in length and parallel. Close the thermal room and connect the NGD circuit to be tested on the no-load cable.
- *Step C:* VNA calibration with respect to the range of the frequency of the CUT.
- *Step D:* Measure the S-parameters of the cable with the temperature change when no load.
- *Step E:* Adjust the room temperature and wait for the temperature stabilization.
- *Step F:* Adjust the temperature box, the range of each rise is 4°C within the time of 5 min. After reaching a rise, keep the temperature stable during 1 min. Then, derive the S-parameter data from the VNA.
- *Step G:* The previous step must be repeated until the temperature variation reaches 40°C. For the present case of the study, the users must save 11 groups of ring-stub circuit S-parameter data families.

To verify the feasibility of the robustness analysis of the NGD circuit under ambient temperature stress, a practical investigation will be presented in the next section.

Investigation on the results of the BP NGD electrothermal experimentation

The present section deals with the examination of the ring-stub circuit electrothermal test results. The BP NGD validation based on the comparison between simulation and measurement is presented. Then, the BP NGD responses will be discussed in the function of the ambient temperature variation.

Principle of the experimental setup for the NGD electrothermal analysis

To validate the BP NGD behavior of the CUT, comparisons between the simulated (“Sim.”) and measured (“Meas.”) results were carried out in the frequency band from 2.35 to 2.5 GHz. The simulated results were obtained from the commercial tool of electronic and RF/microwave circuit simulator ADS® from Keysight Technologies®. The ring-stub circuit operates as a dual-band NGD function. The simulated, and measured GDs and magnitudes of the reflection and transmission coefficients are plotted in Fig. 5(a) and in Fig. 5(b), respectively. It can be pointed out that these comparative results present a very good agreement. In addition, the simulated and measured GD responses are plotted in Fig. 5(c). These results confirm that the ring stub CUT behaves as a BP NGD function. Table 3 presents the comparison between the simulated and experimented results of BP NGD specifications. As expected, the CUT exhibits NGD center frequency of approximately $f_0 = 2.42$ GHz and NGD value, $GD(f_0)$, of -1.9 ns. It can be seen from Fig. 5(b) that in the test frequency band, the attenuation remains better than -4 dB and the reflection coefficient is better than -11 dB. The slight frequency shifts of NGD center frequency are mainly due to the fabrication inaccuracies, substrate effective permittivity tolerance, and losses versus the numerical computation accuracy.

The electrothermal test results of the ring-stub circuit were generated with respect to the guideline indicated in Subsection C of section III. The experimented data results obtained after

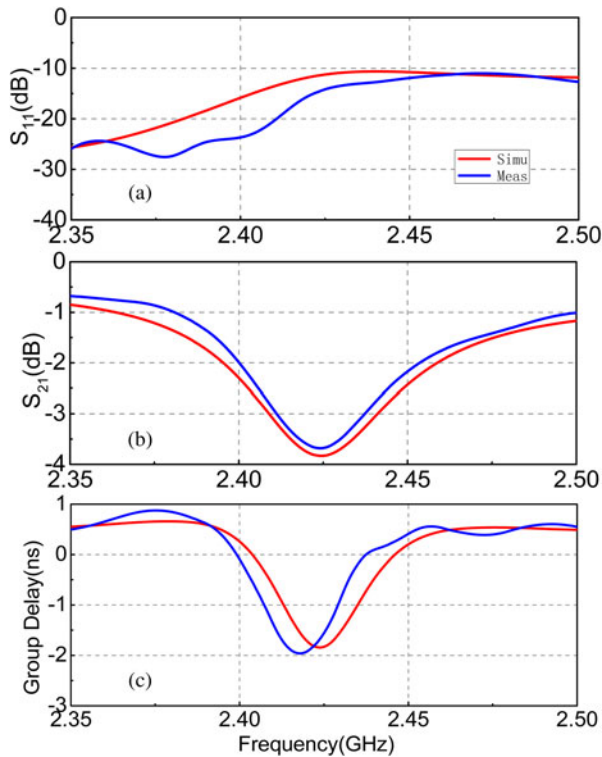


Fig. 5. (a) Reflection and (b) transmission coefficients and (c) GD responses of the ring-stub CUT prototype shown by Figs. 1 in the second bandwidth at $\Delta T=0$.

Table 3. Comparison of BP NGD specifications from the ring-stub CUT

Approach	f_0 (GHz)	$GD(f_0)$ (GHz)	BW (MHz)	$S_{21}(f_0)$ (dB)	$S_{11}(f_0)$ (dB)
Simu.	2.424	-1.85	42.7	-3.83	-11.2
Meas.	2.418	-1.97	38.5	-3.68	-15.9

the post-processing will be analyzed in the two following subsections.

Interconnection cable calibration including the temperature stress effect

Before the NGD characterization of the ring-stub circuit, the interconnection cable was separately calibrated at each sample of the room temperature variation, ΔT , was progressively increased from 0 to 40°C step 1°C. During the test, the VNA was calibrated from 2.3 to 2.6 GHz to generate the thermal and frequency-dependent S-parameters of the employed interconnection cable which can be denoted:

$$[S_{cable}(jf, T)] = \begin{bmatrix} S_{11cable}(jf, T) & S_{21cable}(jf, T) \\ S_{21cable}(jf, T) & S_{11cable}(jf, T) \end{bmatrix} \quad (11)$$

The associated GD determined from the transmission coefficient is given by:

$$GD_{cable}(f, T) = \frac{-\partial \arg [S_{21cable}(jf, T)]}{2\pi \partial f} \quad (12)$$

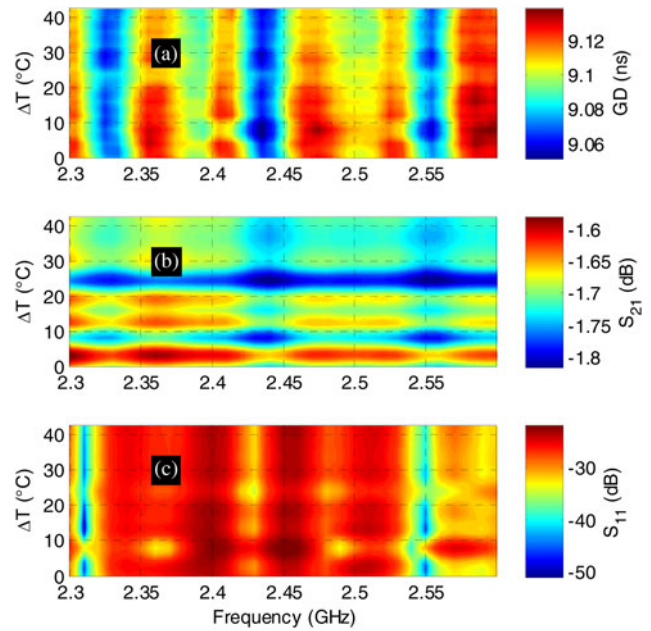


Fig. 6. Mappings of (a) GD, (b) S_{21} and (c) S_{11} for the interconnection cable versus frequency and temperature effect.

Table 4. GD, transmission and reflection coefficients at the NGD center frequency of the interconnected cable

$\Delta T(^{\circ}C)$	f_0 (GHz)	$GD(f_0)$ (GHz)	$S_{21}(f_0)$ (dB)	$S_{11}(f_0)$ (dB)
0	2.434	9.070	-1.725	-27.329
4	2.434	9.064	-1.658	-27.360
8	2.432	9.052	-1.792	-24.292
12	2.429	9.086	-1.676	-28.924
16	2.427	9.082	-1.715	-29.243
20	2.426	9.086	-1.684	-29.135
24	2.425	9.088	-1.794	-32.331
28	2.423	9.084	-1.738	-29.512
32	2.421	9.090	-1.711	-29.587
36	2.418	9.109	-1.709	-26.062
40	2.416	9.115	-1.704	-25.918

Consequently, the obtained electrothermal mappings of the employed interconnection cable GD, transmission and reflection coefficients are displayed in Figs 6(a), 6(b) and 6(c), respectively. Significant variations of the interconnection cable S-parameter magnitudes can be observed. The NGD center frequency, f_0 , of the ring-stub circuit under temperature stress is considered to carry out the calibration. Accordingly, we consider the $GD(f_0)$, $S_{21}(f_0)$, and $S_{11}(f_0)$ empirical data of the tested cable summarized in Table 4. The influence of the interconnection cable can be quantified from this table. It can be emphasized from this empirical result that the cable response presents the variations of:

- Interconnect cable GD presenting medium value of about mean ($GD_{cable}(f_0)$) \approx 9.1 ns and variation $\max(GD_{cable}(f_0))$ - $\min(GD_{cable}(f_0))$ <0.1 ns,

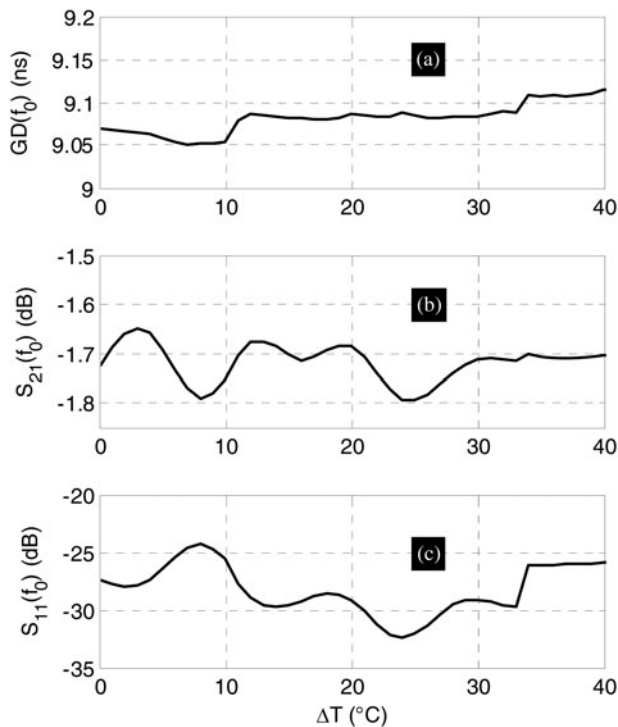


Fig. 7. (a) GD , (b) S_{21} and (c) S_{11} of the interconnection cable at NGD center frequencies versus temperature effect.

- Transmission coefficient having absolute variations of about $\max(S_{21cable}(f_0)) - \min(S_{21cable}(f_0)) < 0.2$ dB,
- And reflection coefficient with maximal value $\max(S_{11cable}(f_0))$ lower than -23 dB.

By taking into account the results of the cable calibration, the BP NGD characterization of the ring-stub circuit including the electrothermal robustness analysis will be discussed in the following paragraph (Fig. 7).

BP NGD characterization after processing at ambient temperature on the ring-stub circuit

The heart of the thermal stress robustness investigation is explored in the present subsection. The robustness study of the BP NGD CUT is focused around the NGD frequency band. We choose the operation frequency band between 2.35 and 2.5 GHz. The following paragraph explains the calibration approach by considering the cable electrothermal effect.

NGD circuit calibration approach by taking into account the cable electrothermal effect response

The electrothermal observable data processing is elaborated from the measurement of the total circuit composed of the interconnection cable characterized in the previous subsection connected to the CUT. Accordingly, the total circuit S-parameters can be denoted by:

$$[S_{total}(jf, T)] = \begin{bmatrix} S_{11total}(jf, T) & S_{21total}(jf, T) \\ S_{21total}(jf, T) & S_{11total}(jf, T) \end{bmatrix} \quad (13)$$

As the interconnection cable with S-parameters given by equation (11) and the tested circuit with S-parameters given by

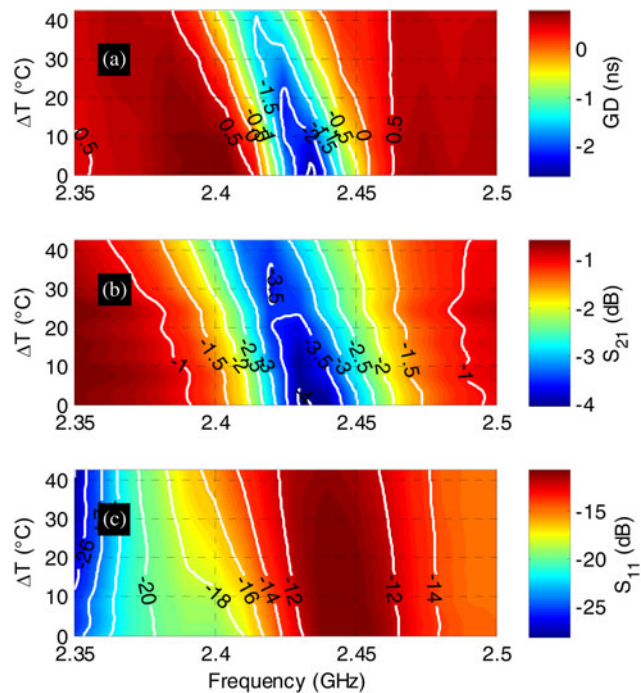


Fig. 8. Mappings of experimented (a) GD , (b) S_{21} and (c) S_{11} of ring-stub circuit versus (f, T) .

equation (10) are very well matched in the NGD frequency band, we can deduce the CUT transmission coefficient from the following relation:

$$S_{11}(jf, T) \approx S_{11total}(jf, T) \quad (14)$$

$$S_{21}(jf, T) \approx \frac{S_{21total}(jf, T)}{S_{21cable}(jf, T)} \quad (15)$$

It can be derived from equation (14) that the ring-stub CUT measured GD and transmission coefficient magnitude in decibel are respectively expressed by:

$$GD(f, T) \approx GD_{total}(f, T) - GD_{cable}(f, T) \quad (16)$$

$$S_{21dB}(f, T) \approx S_{21totaldB}(f, T) - S_{21cabledB}(f, T) \quad (17)$$

Based on the proposed approach, the empirical results are examined in the following paragraph.

Electrothermal data mapping processing of the ring-stub CUT

The thermal stress measurement of the ring-stub circuit was carried out by including the interconnect cable. The experimental data represented by S-parameter equation (10) were recorded after 11 min of the temperature change. After the thermal stress, the BP NGD characterization of the ring NGD circuit is performed by using previously suggested equations (13), (15), and (16). Similar to the analysis of the previous subsection, the analyses were based on the mappings

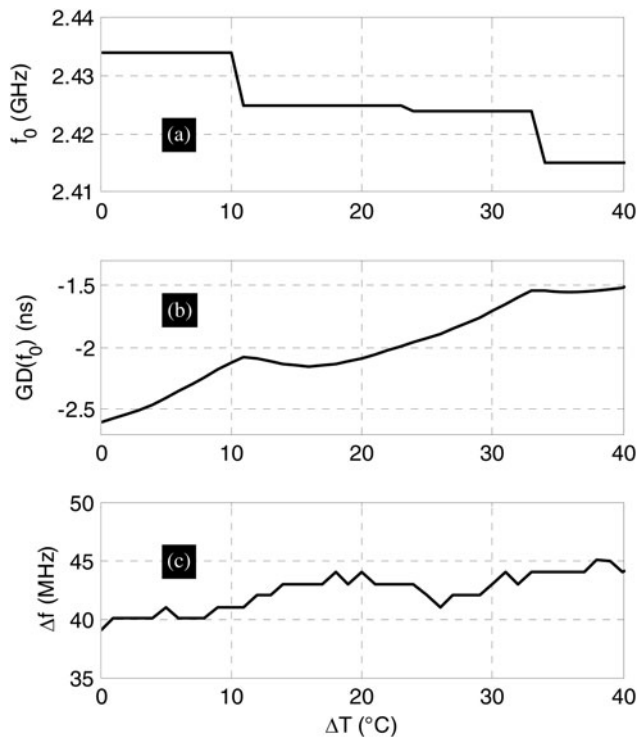


Fig. 9. Plots of NGD (a) center frequency, (b) value and (c) bandwidth versus temperature parameter after test processing of ring-stub circuit.

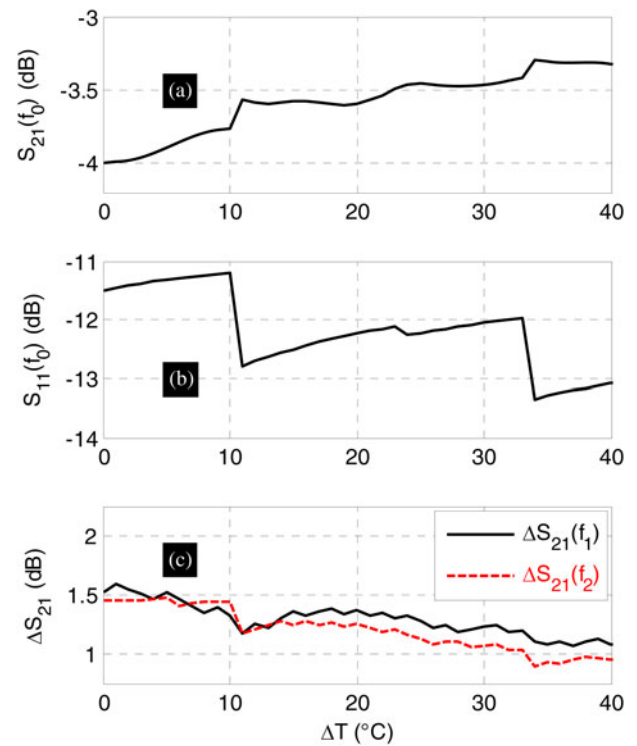


Fig. 10. (a) Transmission and (b) reflection coefficients at the NGD center frequency, and (c) attenuation flatness versus temperature of the ring-stub circuit after test processing value.

of the ring-stub CUT GD, transmission and reflection coefficients displayed by Figs 8(a), 8(b) and 8(c), respectively. As expected, an interesting electrothermal effect is curiously observed. It can be seen in Fig. 8(a) that the ring-stub circuit conserve the BP NGD behavior despite the thermal stress. However, the NGD value and the NGD center frequency are decreasing inversely to the temperature variation. Moreover, it can be underlined from Fig. 8(a) that the NGD bandwidth is slightly increasing. Furthermore, in the NGD frequency range, despite the temperature stress, at the NGD center frequency, the attenuation depicted by Fig. 8(b) remains better than 3 dB and the ring-stub circuit access matching illustrated by Fig. 8(c) remains better than -11 dB.

In addition, similar to the normal operation of BP NGD circuits available in the literature, the transmission coefficient magnitude presents an electrothermal behavioral effect shown by Fig. 8(b) similar to the GD of Fig. 8(a). Based on the explored raw data, the robustness study related to the BP NGD specifications of the ring-stub NGD circuit will be examined in the following paragraph.

Robustness related to the BP NGD specifications

In the area of electronic and microwave engineering, the robustness study must be referenced by observable data. For the present study, we are presenting a BP NGD behavior of a microstrip circuit against thermal stress. For the best of the authors' knowledge, this is the first study of electrothermal BP characterization applied to microstrip circuit.

As aforementioned in Fig. 2, the BP NGD specifications are quantified by the NGD center frequency, NGD value, NGD bandwidth, attenuation and reflection coefficient of the CUT. Based on

the data depicted in Fig. 8, we extracted the NGD center frequency, NGD value, and NGD bandwidth versus stress temperature which are plotted in Figs 9(a), 9(b) and 9(c), respectively. Then, the variations of the transmission coefficient, reflection coefficient, and insertion loss flatness versus stress temperature are shown in Figs 10(a), 10(b) and 10(c).

The overall BP NGD specifications are characterized by the NGD center frequency, f_0 , BW, $\Delta f = f_2 - f_1$, value, $GD(f_0)$, attenuation, $S_{21,db}(f_0)$, matching, $S_{21,db}(f_0)$, and insertion loss flatness, $S_{21,db}(f_1) - S_{21,db}(f_0)$ and $S_{21,db}(f_2) - S_{21,db}(f_0)$. Table 5 recapitulates the quantified BP NGD characteristics of the ring-stub circuit under temperature variation from 0 to 40°C with a step of 4°C.

It is noteworthy from Table 5 that the attenuation and access matching are still better than 4 dB and 11 dB despite the stress. However, we can point out that:

- The NGD center frequency presents a shift of about: $\max(f_0) - \min(f_0) = 18 \text{ MHz}$,
- And the GD maximal variation is of about: $\max[GD(f_0)] - \min[GD(f_0)] = 1.26 \text{ ns}$.

Discussion on the application of BP NGD robustness study of the ring-stub CUT

These previous empirical results enable to qualify the BP NGD robustness of the ring-stub circuit. The main robustness risk related to such results should be specified in the function of the electronic system applications. For example, for the case of the IEEE 802.11a/b wireless transceiver system, the standard communication channel bandwidths are higher than 20 MHz. Therefore,

Table 5. BP NGD specifications of the ring-stub CUT versus temperature

ΔT (°C)	f_0 (GHz)	Δf (MHz)	$GD(f_0)$ (GHz)	$S_{21}(f_0)$ (dB)	$S_{11}(f_0)$ (dB)	$S_{21}(f_1) - S_{21}(f_0)$ (dB)	$S_{21}(f_2) - S_{21}(f_0)$ (dB)
0	2.434	39	-2.914	-4.176	-11.5	1.52	1.45
4	2.434	40	-2.746	-4.098	-11.34	1.46	1.46
8	2.432	40	-2.549	-3.798	-11.26	1.35	1.44
12	2.429	42	-2.472	-3.947	-12.71	1.26	1.21
16	2.427	43	-2.440	-3.805	-12.44	1.33	1.28
20	2.426	44	-2.327	-3.762	-12.23	1.37	1.26
24	2.425	43	-2.181	-3.599	-12.26	1.33	1.17
28	2.423	42	-2.003	-3.602	-12.12	1.19	1.11
32	2.421	43	-1.822	-3.577	-12	1.18	1.03
36	2.418	44	-1.749	-3.511	-13.25	1.11	0.92
40	2.416	44	-1.653	-3.438	-13.1	1.08	0.95

we can expect that the NGD circuit robustness can induce tolerable operation within the ambient temperature variation, ΔT , less than 40°C.

Conclusion

An original study of the BP NGD microstrip circuit, never being achieved before, is investigated. The study is based on the test of the ring-stub microstrip circuit. After the recall of the BP NGD specifications, the NGD design of the PoC is described. Then, the electrothermal test guideline is explained with the consideration of the experimental setup of the thermal room and the VNA calibration.

The experimental test shows that as the temperature increases from 0 to 40°C, the center frequency decreases about 18 MHz, and the GD decreases about 1.3 ns and the S_{21} increases about 0.7 dB. The ring stub circuit still maintains the BP NGD behavior. Despite the existence of stress, the attenuation and access matching are still better than 4 and 11 dB, which proves the BP NGD robustness of the ring stub circuit. Therefore, we can expect when the ambient temperature changes within 40°C, the NGD circuit can maintain good robustness.

The proposed study is useful for the future application of the BP-NGD circuit and the robustness and reliability of the electronic system in a complex environment such as a large ambient temperature variation range.

Acknowledgements. This research work was supported in part by NSFC under Grant 61971230, and in part by the Jiangsu Specially Appointed Professor program and Six Major Talents Summit of Jiangsu Province (2019-DZXX-022) and in part by the Startup Foundation for Introducing Talent of NUIST.

References

1. **Chu S and Wong S** (1982) Linear pulse propagation in an absorbing medium. *Physical Review Letters* **48**, 738–741. doi: 10.1103/PhysRevLett.48.738.
2. **Ségard B and Macke B** (1985) Observation of negative velocity pulse propagation. *Physics Letters A* **109**, 213–216. doi: 10.1016/0375-9601(85)90305-6.
3. **Macke B and Ségard B** (2003) Propagation of light-pulses at a negative group-velocity. *European Physical Journal D: Atomic, Molecular and Optical Physics* **23**, 125–141. doi: 10.1140/epjd/e2003-00022-0.
4. **Munday JN and Robertson WM** (2007) Observation of negative group delays within a coaxial photonic crystal using an impulse response method. *Optics Communications* **273**, 32–36. doi: 10.1016/j.optcom.2006.12.039.
5. **Eleftheriades GV, Siddiqui O and Iyer AK** (2003) Transmission line models for negative refractive index media and associated implementations without excess resonators. *IEEE Microwave and Wireless Components Letters* **13**, 51–53. doi: 10.1109/LMWC.2003.808719.
6. **Siddiqui OF, Mojahedi M and Eleftheriades GV** (2003) Periodically loaded transmission line with effective negative refractive index and negative group velocity. *IEEE Transactions on Antennas and Propagation* **51**, 2619–2625. doi: 10.1109/TAP.2003.817556.
7. **Siddiqui OF, Erickson SJ, Eleftheriades GV and Mojahedi M** (2004) Time-domain measurement of negative group delay in negative-refractive-index transmission-line metamaterials. *IEEE Transactions on Microwave Theory* **52**, 1449–1454. doi: 10.1109/TMTT.2004.827018.
8. **Kokkinos T, Sarris CD and Eleftheriades GV** (2005) Periodic finite-difference time-domain analysis of loaded transmission-line negative-refractive-index metamaterials. *IEEE Transactions on Microwave Theory* **53**, 1488–1495. doi: 10.1109/tmtt.2005.845197.
9. **Markley L and Eleftheriades GV** (2010) Quad-band negative-refractive-index transmission-line unit cell with reduced group delay. *Electronics Letters* **46**, 1206–1208. doi: 10.1049/el.2010.1797.
10. **Monti G and Tarricone L** (2009) Negative group velocity in a split ring resonator-coupled microstrip line. *Progress in Electromagnetics Research* **94**, 33–47. doi: 10.2528/PIER09052801.
11. **Nesimoglu T and Sabah C** (2016) A tunable metamaterial resonator using varactor diodes to facilitate the design of reconfigurable microwave circuits. *IEEE Transactions on Circuits and Systems II* **63**, 89–93. doi: 10.1109/TCSII.2015.2503058.
12. **Barroso JJ, Oliveira JEB, Coutinho OL and Hasar UC** (2016) Negative group velocity in resistive lossy left-handed transmission lines. *IET Microwaves, Antennas & Propagation* **10**, 808–815. doi: 10.1049/iet-map.2017.0357.
13. **Cao H, Dogariu A and Wang LJ** (2003) Negative group delay and pulse compression in superluminal pulse propagation. *IEEE Journal of Selected Topics in Quantum Electronics* **9**, 52–58. doi: 10.1109/JSTQE.2002.807974.
14. **Macke B, Ségard B and Wielonsky F** (2005) Optimal superluminal systems. *Physical Review E* **72**, 035601(R). doi: 10.1103/PhysRevE.72.035601.
15. **Ségard B and Macke B** (2008) Two-pulse interference and superluminality. *Optics Communications* **281**, 12–17. doi: 10.1016/j.optcom.2007.09.007.

16. **Kitano M, Nakanishi T and Sugiyama K** (2003) Negative group delay and superluminal propagation: an electronic circuit approach. *IEEE Journal of Selected Topics in Quantum Electronics* **9**, 43–51. doi: 10.1109/JSTQE.2002.807979.
17. **Mitchell MW and Chiao RY** (1997) Negative group delay and “fronts” in a causal system: an experiment with very low-frequency bandpass amplifiers. *Physics Letters A* **230**, 133–138. doi: 10.1016/S0375-9601(97)00244-2.
18. **Mitchell MW and Chiao RY** (1998) Causality and negative group-delays in a simple bandpass amplifier. *American Journal of Physics* **66**, 14–19. doi: 10.1119/1.18813.
19. **Ravelo B** (Oct. 2014) Similitude between the NGD function and filter gain behaviours. *International Journal of Circuit Theory and Applications* **42**, 1016–1032. doi: 10.1002/cta.1902.
20. **Wu C-T-M and Itoh T** (2014) Maximally flat negative group-delay circuit: a microwave transversal filter approach. *IEEE Transactions on Microwave Theory* **62**, 1330–1342. doi: 10.1109/TMTT.2014.2320220.
21. **Zhang T, Xu R and Wu CM** (2017) Unconditionally stable non-foster element using active transversal-filter-based negative group delay circuit. *IEEE Microwave and Wireless Components Letters* **27**, 921–923. doi: 10.1109/LMWC.2017.2745487.
22. **Qiu L-F, Wu L-S, Yin W-Y and Mao J-F** (2017) Absorptive bandstop filter with prescribed negative group delay and bandwidth. *IEEE Microwave and Wireless Components Letters* **27**, 639–641. doi: 10.1109/LMWC.2017.2711572.
23. **Wang Z, Cao Y, Shao T, Fang S and Liu Y** (2018) A negative group delay microwave circuit based on signal interference techniques. *IEEE Microwave and Wireless Components Letters* **28**, 290–292. doi: 10.1109/LMWC.2018.2811254.
24. **Liu G and Xu J** (2017) Compact transmission-type negative group delay circuit with low attenuation. *Electronics Letters* **53**, 476–478. doi: 10.1049/el.2017.0328.
25. **Shao T, Wang Z, Fang S, Liu H and Fu S** (2017) A compact transmission line self-matched negative group delay microwave circuit. *IEEE Access* **5**, 22836–22843. doi: 10.1109/ACCESS.2017.2761890.
26. **Chaudhary G, Jeong Y and Lim J** (2014) Miniaturized dual-band negative group delay circuit using dual-plane defected structures. *IEEE Microwave and Wireless Components Letters* **24**, 521–523. doi: 10.1109/LMWC.2014.2322445.
27. **Shao T, Fang S, Wang Z and Liu H** (2018) A compact dual-band negative group delay microwave circuit. *Radio Engineering* **27**, 1070–1076. doi: 10.13164/re.2018.1070.
28. **Wan F, Li N and Ravelo B** (2020) O = O shape low-loss negative group delay microstrip circuit. *IEEE Transactions on Circuits and Systems II* **67**, 1795–1799. doi: 10.1109/TCSII.2019.2955109.
29. **Zhou X, Gu T, Wu L, Wan F, Li B, Murad NM, Lalléchére S and Ravelo B** (2020) S-Matrix and bandpass negative group delay innovative theory of Ti-geometrical shape microstrip structure. *IEEE Access* **8**, 160363–160373. doi: 10.1109/ACCESS.2020.3020270.
30. **Ahn K-P, Ishikawa R and Honjo K** (2009) Group delay equalized UWB InGaP/GaAs HBT MMIC amplifier using negative group delay circuits. *IEEE Transactions on Microwave Theory* **57**, 2139–2147. doi: 10.1109/TMTT.2009.2027082.
31. **Shao T, Wang Z, Fang S, Liu H and Chen Z** (2020) A full-passband linear-phase band-pass filter equalized with negative group delay circuits. *IEEE Access* **8**, 43336–43343. doi: 10.1109/ACCESS.2020.2977100.
32. **Ravelo B, Thakur A, Saini A and Thakur P** (2015) Microstrip dielectric substrate material characterization with temperature effect. *Applied Computational Electromagnetics* **30**, 1322–1328.
33. **Ravelo B** (2018) Multiphysics model of microstrip structure under high voltage pulse excitation. *IEEE Journal on Multiscale and Multiphysics Computational Techniques* **3**, 88–96. doi: 10.1109/JMMCT.2018.2852681.
34. **Xu Z, Ravelo B and Maurice O** (2019) Multiphysics tensorial network analysis applied to PCB interconnect fatigue under thermal cycle aggression. *IEEE Transactions on Electromagnetic Compatibility* **61**, 1253–1260. doi: 10.1109/TEMC.2019.2911873.
35. **Thermal room specifications, ESPEC**. Available at <https://www.espec.cn>.



Hongyu Du received the B.Eng. degree in communication engineering from the Nanjing University of Information Science and Technology, Nanjing, China, in 2018. She is currently working toward a Master degree from Nanjing University of Information Science and Technology. Her research interests include abnormal wave propagation in dispersive media and microwave circuits.



Fayu Wan received the Ph.D. degree in electronic engineering from the University of Rouen, Rouen, France, in 2011. From 2011 to 2013, he was a Postdoctoral Fellow with the Electromagnetic Compatibility Laboratory, Missouri University of Science and Technology, Rolla, MO, USA. He is currently a Full Professor at the School of Electronics and Information Engineering, Nanjing University of Information Science and Technology, Nanjing, China. His current research interests include negative group delay (NGD) circuits, electrostatic discharge, electro-magnetic compatibility, and advanced RF measurement.



Sébastien Lalléchére received the Ph.D. Degree in electronics/electromagnetism from Université Blaise Pascal, Clermont-Ferrand, France, in 2006. He is currently an Associate Professor at Institut Pascal and Université Clermont Auvergne, France. His research interests cover the fields of electromagnetic compatibility including complex electromagnetic environments, electromagnetic coupling, and computational electromagnetics.



Wencelas Rahajandraibe received the B.Sc. degree in electrical engineering from Nice Sophia-Antipolis University, France, in 1996, the M.Sc. Degree (Hons.) in electrical engineering from the Science Department, University of Montpellier, France, in 1998, and the Ph.D. degree in microelectronics from the University of Montpellier. He is currently a Full Professor at the University of Aix-Marseille, France. In 1998, he joined the Informatics, Robotics and Microelectronics Laboratory of Montpellier (LIRMM), Microelectronics Department. In 2003, he joined the Materials, Microelectronics and Nanoscience Laboratory of Provence (IM2NP), Micro electronic Department, Marseille, France, where he was an Associate Professor. Since 2014, he has been a Professor with Aix Marseille University, where he heads the IM2NP Laboratory, Integrated Circuit Design Group. His research interests include the design of analog and RF IC's for telecommunication systems and for smart sensor ultra-low-power IC interfaces.



Blaise Ravelo is currently a Full Professor with the Nanjing University of Information Science and Technology (NUIST), Nanjing, China. He is a Lecturer on circuit and system theory, and STEM (science, technology, engineering, and maths) and applied physics. He is also a pioneer of the negative group delay (NGD) concept about $t < 0$ signal travelling physical space. This extraordinary concept is potentially useful for anticipating and predicting all kinds of information. With the USA, Chinese, Indian, European, and African partners, he is actively involved and contributes to several international research projects, such as ANR, FUI, FP7, INTERREG, H2020, Euripides2, Eurostars, and so on. He coauthored more than 340 scientific research papers on new technologies published in international conferences and journals. His research interests include multiphysics and electronics engineering. He has been a member of the Scientific Technical Committee of Advanced Electromagnetic Symposium (AES), since 2013.